

# The effect of point sources on satellite observations of the cosmic microwave background

M.P. Hobson<sup>1</sup>, R.B. Barreiro<sup>2,3</sup>, L. Toffolatti<sup>4,5</sup>, A.N. Lasenby<sup>1</sup>, J.L. Sanz<sup>2</sup>,  
A.W. Jones<sup>1</sup> and F.R. Bouchet<sup>6</sup>

<sup>1</sup> *Astrophysics Group, Cavendish Laboratory, Madingley Road, Cambridge CB3 0HE, UK*

<sup>2</sup> *Instituto de Física de Cantabria (CSIC-UC), Facultad de Ciencias, Av. de Los Castros s/n, Santander 39005, SPAIN*

<sup>3</sup> *Departamento de Física Moderna, Universidad de Cantabria, Facultad de Ciencias, Av. de Los Castros s/n, Santander 39005, SPAIN*

<sup>4</sup> *Osservatorio Astronomico, Vicolo dell'Osservatorio 5, 35122 Padova, ITALY*

<sup>5</sup> *Departamento de Física, Universidad de Oviedo, c.le Calvo Sotelo s/n, 33007 Oviedo, SPAIN*

<sup>6</sup> *Institut d'Astrophysique de Paris, 98 bis Boulevard Arago, 75014 Paris, FRANCE*

Accepted ????. Received ????. in original form 7 May 2019

## ABSTRACT

We study the effect of extragalactic point sources on satellite observations of the cosmic microwave background (CMB). In order to separate the contributions due to different foreground components, a maximum-entropy method is applied to simulated observations by the Planck Surveyor satellite. In addition to point sources, the simulations include emission from the CMB and the kinetic and thermal Sunyaev-Zel'dovich (SZ) effects from galaxy clusters, as well as Galactic dust, free-free and synchrotron emission. We find that the main input components are faithfully recovered and, in particular, that the quality of the CMB reconstruction is only slightly reduced by the presence of point sources. In addition, we find that it is possible to recover accurate point source catalogues at each of the Planck Surveyor observing frequencies.

**Key words:** methods: data analysis – techniques: image processing – cosmic microwave background.

## 1 INTRODUCTION

A new generation of cosmic microwave background (CMB) satellite missions are currently in the final stages of design. The NASA MAP satellite is expected to be launched by 2000, followed by the ESA Planck Surveyor in 2007 (Bersanelli et al. 1996). Both missions will provide detailed all-sky maps of the CMB anisotropies, leading to definitive measurements of the CMB power spectrum. This should allow tight constraints to be placed on fundamental cosmological parameters and distinguish between competing theories of structure formation in the early Universe such as inflation and topological defects.

The maps produced by these satellites will, however, contain contributions from various foreground components, most notably Galactic dust, free-free and synchrotron emission as well as the kinetic and thermal SZ effects from galaxy clusters. In addition, significant contamination from extragalactic point sources is also expected. It is therefore clear that in order to obtain maps of the CMB anisotropies alone, it is necessary to separate the emission due to these various components.

In a previous paper, Hobson et al. (1998) (hereafter Paper I) use a non-linear maximum-entropy method (MEM) to separate the emission due to the different foreground components from simulated Planck Surveyor observations of a  $10 \times 10 \text{ deg}^2$  field (see

Bouchet et al. 1997; Gispert & Bouchet 1997). It was found that faithful reconstructions may be produced not only of the CMB anisotropies but also of the Galactic components and the kinetic and thermal SZ effects from massive clusters. The analysis presented in Paper I does not, however, include the effect of extragalactic point sources, since no reliable simulations were available at that time.

In this paper, we apply a generalised version of the MEM separation algorithm to simulated Planck Surveyor observations that also include a population of point sources. This allows us to assess the effect of point sources on the accuracy with which the CMB anisotropies and foreground components can be recovered. The simulated maps of the point sources were created for each Planck Surveyor observing frequency using the updated number counts in each frequency band predicted by Toffolatti et al. (1998). These predictions are based on the Danese et al. (1987) model for the evolution of radio selected sources (adopting an average spectral index  $\alpha = 0$  for compact flat-spectrum sources up to  $\simeq 200$  GHz and a break to  $\alpha = 0.7$  at higher frequencies) and on the model C of Franceschini et al. (1994) for the evolution of far-IR selected sources, updated by Burigana et al. (1997) to account for the isotropic sub-mm component estimated by Puget et al. (1996). The point source map at each frequency was produced by Poisson distributing all the sources in the  $10^{-5} \text{ Jy} < S(\nu) < 10 \text{ Jy}$  flux range.

Unless sources are identified and subtracted down to faint flux limits, the contribution of clustered sources to the CMB anisotropies is generally found to be small in comparison with the Poisson term. As discussed by Toffolatti et al. (1998), far-IR selected sources should dominate the number counts of bright objects at frequencies  $\nu > 300$  GHz, whereas radio selected sources should dominate at lower frequencies. The two underlying parent populations are largely different and uncorrelated, consisting of normal spirals and starburst galaxies in the far-IR and mostly compact AGN, blazars and quasars in the radio.

## 2 THE SEPARATION ALGORITHM

Our aim is to reconstruct the CMB anisotropies and the foreground components in the presence of both instrumental noise and contamination due to extragalactic point sources. A straightforward initial step might be to subtract the point-source contribution from those pixels that are obviously contaminated. The procedure can, however, lead to difficulties, since a particular contaminated pixel can usually only be identified in a few of the frequency channels. Therefore, since the spectral behaviour of point sources is generally rather complicated, any interpolation between frequencies must be performed with caution. An alternative Fourier-filter approach to removing point sources from CMB maps has been proposed by Tegmark & de Oliveira-Costa (1998).

In our approach, we do not remove any contaminated pixels from the simulated data. Instead, we consider the point sources as an additional contribution to the ‘noise’ and allow the generalised version of the MEM algorithm to reconstruct the CMB and foreground emission in the presence of the point sources. The MEM technique is discussed in detail in Paper I and so here we will outline the basic points and instead concentrate on how to address the effect of point sources within the existing formalism.

At any given frequency  $\nu$ , the total rms temperature fluctuation on the sky in a direction  $\hat{x}$  is given by the superposition of the physical components. In Fig. 1 we show the  $10 \times 10$  deg<sup>2</sup> simulated input maps for all the different physical components (except the point sources) at a reference frequency  $\nu_0 = 300$  GHz; each map consists of  $400 \times 400$  pixels and has been convolved with a Gaussian beam with a FWHM of 4.5 arcmin, which is the highest angular resolution of the Planck Surveyor satellite. The cell size for each map is 1.5 arcmin.

If we observe the microwave sky in a given direction  $\hat{x}$  at  $n_f$  different frequencies, we obtain an  $n_f$ -component data vector that contains the observed temperature fluctuations in this direction at each observing frequency plus instrumental noise. The  $\nu$ th component of the data vector in the direction  $\hat{x}$  may be written as (see Paper I)

$$d_\nu(\hat{x}) = \sum_{j=1}^{N_p} P_\nu(|\hat{x} - \hat{x}_j|) \sum_{p=1}^{n_c} F_{\nu p} s_p(\hat{x}_j) + \eta_\nu(\hat{x}) + \epsilon_\nu(\hat{x}), \quad (1)$$

where  $N_p$  denotes the number of pixels in each of the simulated input maps shown in Fig. 1. In this expression we have chosen to separate the contributions from the six physical components shown in Fig. 1 and the point sources. The former are collected together in a signal vector with  $n_c = 6$  components, such that  $s_p(\hat{x})$  is the signal from the  $p$ th physical component at the reference frequency  $\nu_0 = 300$  GHz. The corresponding total emission at the observing frequency  $\nu$  is then obtained by multiplying the signal vector by the  $n_f \times n_c$  frequency response matrix  $F_{\nu p}$  that includes the spectral behaviour of the considered components as well as the transmission

of the  $\nu$ th frequency channel. This contribution is then convolved with the beam profile  $P_\nu(\hat{x})$  of the relevant channel. Since the spectral dependence of the point sources is very complicated, we cannot factorize their contribution in this way and so they are added into the formalism an extra ‘noise’ term. Thus  $\eta_\nu$  is the contribution from point sources as observed by the Planck Surveyor satellite at the frequency  $\nu$ . Finally,  $\epsilon_\nu$  is the expected level of instrumental noise in the  $\nu$ th frequency channel and is assumed to be Gaussian and isotropic. Figs 2 and 3 show the simulated maps at each observing frequency for the LFI and HFI respectively. The simulated data are identical to those presented in Paper I, but also include the point source simulations of Toffolatti et al. (1998).

The assumption of a spatially-invariant beam profile in (1) allows us to perform the reconstruction more effectively by working in Fourier space, since we may consider each  $k$ -mode independently (see Paper I). Thus, in matrix notation, at each mode we have

$$\mathbf{d} = \mathbf{R}\mathbf{s} + \boldsymbol{\eta} + \boldsymbol{\epsilon} = \mathbf{R}\mathbf{s} + \boldsymbol{\zeta}, \quad (2)$$

where  $\mathbf{d}$ ,  $\boldsymbol{\eta}$  and  $\boldsymbol{\epsilon}$  are column vectors each containing  $n_f$  complex components and  $\mathbf{s}$  is a column vector containing  $n_c$  complex components. In the second equality we have combined the instrumental noise vector  $\boldsymbol{\epsilon}$  and the point-source contribution  $\boldsymbol{\eta}$  into a single vector ‘noise’ vector  $\boldsymbol{\zeta}$ . The response matrix  $\mathbf{R}$  and has dimensions  $n_f \times n_c$  and its elements are given by  $R_{\nu p}(k) = \tilde{P}_\nu(k)F_{\nu p}$ .

As discussed in Paper I, the MEM formalism should not itself induce correlations between elements of the reconstructed signal vector. However, the elements of the signal vector  $\mathbf{s}$  at each Fourier mode may well be correlated, this correlation being described by the  $n_c \times n_c$  signal covariance matrix  $\mathbf{C}$  defined by

$$\mathbf{C}(k) = \langle \mathbf{s}(k)\mathbf{s}^\dagger(k) \rangle, \quad (3)$$

where the dagger denotes the Hermitian conjugate. At each Fourier mode, the  $p$ th diagonal element contains the value of the ensemble-averaged power spectrum of the  $p$ th physical component at the reference frequency  $\nu_0$ . Moreover, if prior information is available concerning these correlations, we would wish to include it in our analysis. We therefore introduce the vector of ‘hidden’ variables  $\mathbf{h}$ , related to the signal vector by

$$\mathbf{s} = \mathbf{L}\mathbf{h}, \quad (4)$$

where the  $n_c \times n_c$  lower triangular matrix  $\mathbf{L}$  is obtained by performing a Cholesky decomposition of the signal covariance matrix  $\mathbf{C} = \mathbf{L}\mathbf{L}^\dagger$ . The reconstruction is then performed entirely in terms of  $\mathbf{h}$  and the corresponding reconstructed signal vector is subsequently found using (4).

Using Bayes’ theorem, we choose as our estimator  $\hat{\mathbf{h}}$  of the hidden vector to be that which maximises the posterior probability given by

$$\Pr(\mathbf{h}|\mathbf{d}) \propto \Pr(\mathbf{d}|\mathbf{h})\Pr(\mathbf{h}) \quad (5)$$

where  $\Pr(\mathbf{d}|\mathbf{h})$  is the likelihood of obtaining the data given a particular hidden vector and  $\Pr(\mathbf{h})$  is the prior probability that codifies our expectations about the hidden vector before acquiring any data.

We assume an entropic prior probability for the hidden vector  $\mathbf{h}$  of the form

$$\Pr(\mathbf{h}) \propto \exp[\alpha S(\mathbf{h}, \mathbf{m})] \quad (6)$$

where  $S(\mathbf{h}, \mathbf{m})$  is the cross entropy of the complex vectors  $\mathbf{h}$  and  $\mathbf{m}$ , where  $\mathbf{m}$  is a model vector to which  $\mathbf{h}$  defaults in absence of data. The form of the cross entropy for complex images and the Bayesian

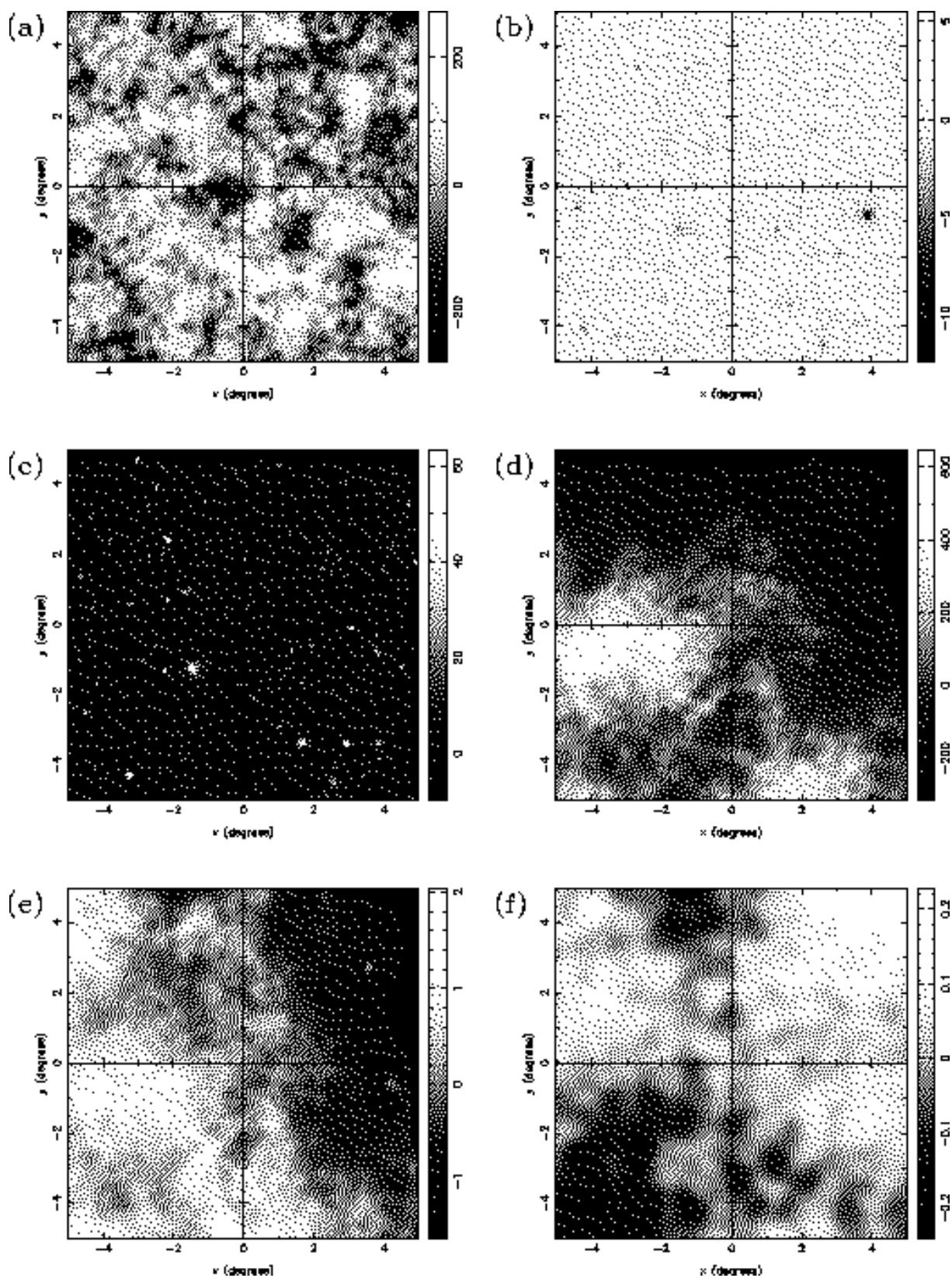


**Figure 1.** The  $10 \times 10 \text{ deg}^2$  realizations of the six input components used to make simulated Planck Surveyor observations: (a) primary CMB fluctuations; (b) kinetic SZ effect; (c) thermal SZ effect; (d) Galactic dust; (e) Galactic free-free; (f) Galactic synchrotron emission. Each component is plotted at 300 GHz and has been convolved with a Gaussian beam of FWHM equal to 4.5 arcmin, the maximum angular resolution proposed for the Planck Surveyor. The map units are equivalent thermodynamic temperature in  $\mu\text{K}$ .

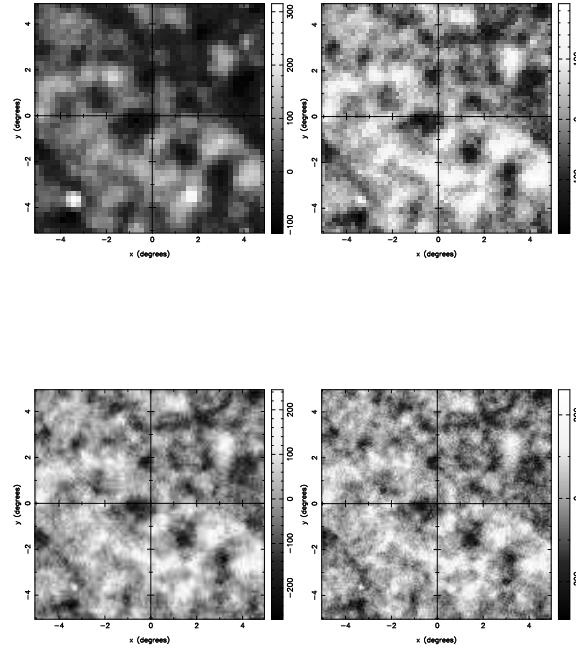


**Figure 2.** The  $10 \times 10 \text{ deg}^2$  maps observed at each of the four observing frequencies of the Planck Surveyor Low Frequency Instrument (LFI): (a) 30 GHz, (b) 44 GHz, (c) 70 GHz, (d) 100 GHz. At each frequency we assume a Gaussian beam with the appropriate FWHM and a sampling rate of FWHM/2.4. Isotropic noise with the relevant rms has been added to each map. The map units are equivalent thermodynamic temperature in  $\mu\text{K}$ .

method for fixing the regularising parameter  $\alpha$  are discussed in Paper I.

Let us now turn our attention to the form of the likelihood function  $\Pr(\mathbf{d}|\mathbf{h})$  in Bayes' theorem (5). In the presence of instrumental noise alone, it is reasonable to assume that the noise contribution is well described by a Gaussian distribution, but in our case the noise term also contains a contribution from the point sources, and so we might expect that a Poisson distribution would be more appropriate for this component. However, since we are performing the reconstruction in the Fourier domain, the noise on each  $k$ -mode will contain contributions from a wide range of scales. Therefore, provided the point sources are distributed on the sky in a statistically-homogeneous manner, we would expect from the central limit theorem that the noise in the Fourier domain is described, at least approximately, by a Gaussian distribution. Therefore, we assume that the likelihood function is given by

$$\begin{aligned} \Pr(\mathbf{d}|\mathbf{h}) &\propto \exp\left(-\boldsymbol{\zeta}^\dagger \mathbf{N}^{-1} \boldsymbol{\zeta}\right) \\ &\propto \exp\left[-(\mathbf{d} - \mathbf{R}\mathbf{L}\mathbf{h})^\dagger \mathbf{N}^{-1} (\mathbf{d} - \mathbf{R}\mathbf{L}\mathbf{h})\right] \end{aligned} \quad (7)$$

where in the last line we have used (2). The noise covariance matrix  $\mathbf{N}$  has dimensions  $n_f \times n_f$  and at any given  $k$ -mode is given by

$$\mathbf{N}(k) = \langle \boldsymbol{\zeta}(k) \boldsymbol{\zeta}^\dagger(k) \rangle. \quad (8)$$

Therefore, at a given Fourier mode, the  $v$ th diagonal element of  $\mathbf{N}$  contains the ensembled-averaged power spectrum at that mode of the instrumental noise plus the point source contribution to the  $v$ th frequency channel. The off-diagonal terms give the cross-correlations between different channels; if the noise is uncorrelated between channels, only the point sources contribute to the off-diagonal elements.

The argument of the exponential in the likelihood function (7) may be identified as (minus) the standard  $\chi^2$  misfit statistic, so we may write  $\Pr(\mathbf{d}|\mathbf{h}) \propto \exp[-\chi^2(\mathbf{h})]$ . Substituting this expression, to-

gether with that for the prior probability given in (6), into Bayes' theorem, we find that maximising the posterior probability  $\Pr(\mathbf{h}|\mathbf{d})$  with respect to  $\mathbf{h}$  is equivalent to minimising the function

$$\Phi(\mathbf{h}) = \chi^2(\mathbf{h}) - \alpha S(\mathbf{h}, \mathbf{m}).$$

This minimisation can be performed using a variable metric minimiser (Press et al. 1994) and requires only a few minutes of CPU time on a Sparc Ultra workstation.

### 3 APPLICATION TO SIMULATED OBSERVATIONS

We now apply the MEM analysis outlined above to the simulated Planck Surveyor data shown in Figs 2 and 3. Clearly, the quality of the reconstructions will depend on our prior knowledge of the input components. Following Paper I, we assume that the frequency spectrum behaviour of the components is accurately known, but we consider two extreme cases relating to our knowledge of the power spectra of the input components and the confusion noise due to point sources.

For the six input components shown in Fig. 1, any prior power spectrum information may be incorporated into the algorithm through the signal covariance matrix  $\mathbf{C}$  given in (3). Strictly speaking, since we are in fact reconstructing the vector of hidden variables  $\mathbf{h}$ , rather than the signal vector  $\mathbf{s}$ , this information actually resides in the matrix  $\mathbf{L}$  given in (4). Similarly, any knowledge of the correlation structure of the instrumental noise and point source contamination can be included via the noise covariance matrix  $\mathbf{N}$ .

#### 3.1 Reconstructions with full power spectrum information

As our first case, we assume knowledge of the azimuthally-averaged power spectra of all six input components in Fig. 1, together with the azimuthally-averaged cross power spectra between components; these contain cross-correlation information in Fourier

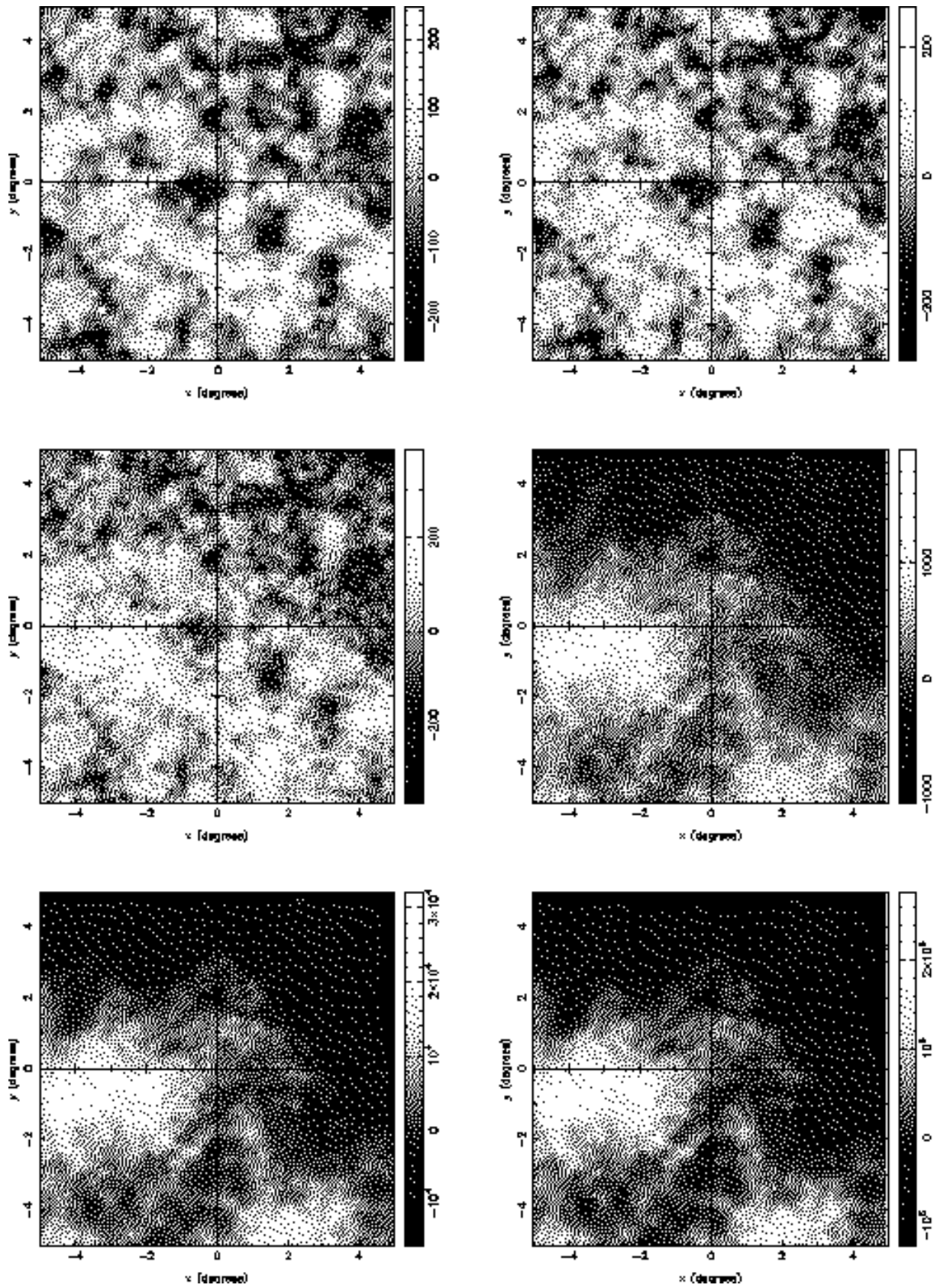


**Figure 3.** As in Fig. 2, but for the six observing frequencies of the Planck Surveyor High Frequency Instrument (HFI): (a) 100 GHz, (b) 143 GHz, (c) 217 GHz, (d) 353 GHz, (e) 545 GHz, (f) 857 GHz.

**Table 1.** The rms of the residuals per 4.5 arcmin FWHM Gaussian beam (in  $\mu\text{K}$ ) of the MEM reconstructions in the presence and absence of point sources, assuming full power spectrum information.

Component	$e_{\text{rms}}$ no sources	$e_{\text{rms}}$ with sources
CMB	5.90	7.50
Kinetic SZ	0.85	0.86
Thermal SZ	3.90	4.40
Dust	1.60	3.80
Free-Free	0.30	0.38
Synchrotron	0.05	0.06

space, so that the matrix  $\mathbf{L}$  is fully specified. We also assume that the noise covariance matrix  $\mathbf{N}$  is fully specified as follows. In addition to the (diagonal) part of the noise matrix due to the instrumental noise, we calculate an empirical estimate of the contribution (to the diagonal and off-diagonal elements) of the point sources. This estimate is calculated directly from 10 independent realizations of the point source maps at each of the 10 Planck Surveyor frequency channels.

The resulting MEM reconstructions of the physical components are shown in Fig. 4 and are plotted on the same greyscale as in Fig. 1 to allow a straightforward comparison with the true input maps. We see that the main input components are faithfully reconstructed, except for a few contaminated pixels containing the brightest point sources. Perhaps most notable is the fact that the majority of contaminating point sources present in the data maps, shown in Fig. 2 and 3, are *not* present in the reconstructions.

In particular, the CMB has been reproduced extremely accurately and is virtually indistinguishable from the true input map, apart from a spurious bright point source in the lower left-hand corner of the reconstruction. As we might expect the dust emission is also accurately recovered, and contains none of the numerous point sources present in the high-frequency data maps shown in Fig. 3. The free-free emission, which is highly correlated with the dust, has also been reconstructed reasonably accurately and displays no evidence of point source contamination. The recovery of the synchrotron emission is, however, somewhat poorer. Although the main features of the true input map are recovered, the reconstruction contains obvious residual point sources. Perhaps most impressive is the reconstruction of the thermal SZ effect, since the MEM algorithm has been successful in reproducing the effect in most of the bright clusters and has misidentified only a few point sources as clusters. At the reference frequency of 300 GHz, these misidentified point sources appear mostly as negative features. The kinetic SZ effect has also been reconstructed in a number of clusters having bright thermal SZ effects. In fact, the quality of the kinetic SZ reconstruction is similar to that obtained in Paper I.

In order to quantify the effect of point sources on the accuracy of the reconstructions, in Table 1 we compare the rms residuals,  $e_{\text{rms}}$ , per 4.5 arcmin FWHM Gaussian beam, of the reconstructions in Fig. 4 with those obtained in Paper I in the absence of point sources. As we might expect, for each component the value of  $e_{\text{rms}}$  is slightly larger when the effects of point sources are included, but the errors are still reasonable small. In particular, we note that the rms error on the CMB reconstruction only increases from 5.9 to 7.5  $\mu\text{K}$ .

As an intermediate case, reconstructions were also performed assuming that only the diagonal elements of the noise covariance matrix were non-zero. This therefore includes information about

the power spectra of the instrumental noise and point source maps at each observing frequency, but ignores any cross-correlation of the point source between frequencies. In this case, the quality of the reconstructed maps is only slightly worse and, in particular, the rms of the residuals in the CMB reconstruction increases marginally to 8.3  $\mu\text{K}$ .

In Fig. 5 we plot the power spectra of the reconstructed maps (faint lines) and compare them with the power spectra of the true input maps (bold lines) as shown in Fig. 1. We see from Fig. 5 that, in spite of the contamination due to point sources, the power spectrum of the MEM reconstruction of the CMB component (panel a) is accurate up to  $\ell \approx 2000$ , at which point the reconstruction begins to underestimate the true power spectrum. For the kinetic SZ effect (panel b) the power spectrum of the reconstruction underestimates the true spectrum at all multipoles, but for the thermal SZ effect (panel c) the reconstructed spectrum follows the true one up to  $\ell \approx 1000$ . The most accurately reconstructed power spectrum is that of the Galactic dust emission (panel d), which closely follows the true spectrum up to  $\ell \approx 3000$ . Finally, the power spectra of the free-free and synchrotron reconstructions (panels e and f) slightly underestimate the true spectra across all multipoles. It was further found that assuming a diagonal noise covariance matrix did not appreciably alter the results. As discussed in Paper I, the errors on the reconstructed power spectra may be easily calculated, and we find that in each case the 68 percent confidence limits on the reconstructed power spectra encompass the true power spectrum at all multipoles.

### 3.2 Reconstructions with no power spectrum information

For our second case, we take the opposite view to that adopted above and assume that almost no power spectrum information is available. This corresponds to assuming a flat (white-noise) power spectrum for each component out to the highest measured Fourier mode. The levels of the flat power spectra are chosen so that the total power in each component is approximately that observed in the input maps in Fig. 1. Furthermore, the noise covariance matrix contains only the diagonal contribution from the instrumental noise, and no attempt is made to include the effects due to point source contamination. As discussed in Paper I, when no power spectrum information is assumed, the MEM algorithm is iterated by using the current reconstructions to update the ICF matrix  $\mathbf{L}$  before embarking on the next iteration. The solution was found to converge after 8 such iterations.

The resulting reconstructions are shown in Fig. 6. In this case, it is most encouraging that the CMB reconstruction is still very accurate, even for this very pessimistic scenario. Once again the reconstruction is, at least by eye, almost indistinguishable from the true map shown in Fig. 1, except for the presence of a very bright point source in the lower left-hand corner of the map. We also see that the Galactic dust component is accurately recovered and contains very few of the point sources present in the high-frequency channel maps shown in Fig. 3. The thermal SZ effect has also been recovered, but only in the brightest clusters, and the reconstruction also contains numerous misidentified point sources that appear as sharp negative features. The reconstructions of the remaining three components are very poor. In particular, the kinetic SZ reconstruction has simply defaulted to zero in the absence of any useful data, whereas the reconstructions of the Galactic free-free and synchrotron emission are heavily contaminated with point sources and no obvious features in the true input maps have been recovered.

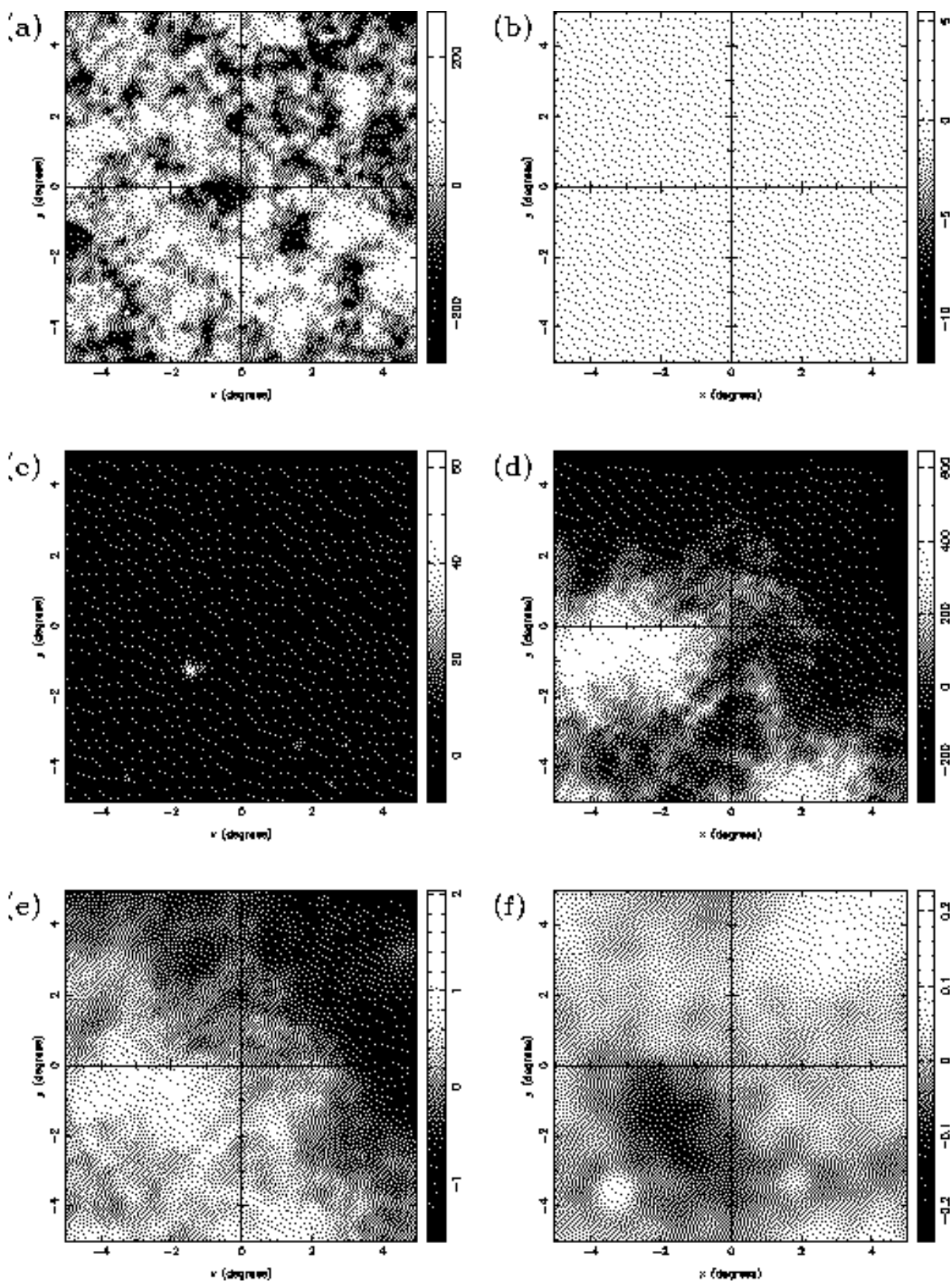


**Figure 4.** MEM reconstruction of the  $10 \times 10 \text{ deg}^2$  maps of the six input components shown in Fig. 1, using full power spectrum information (see text). The components are: (a) primary CMB fluctuations; (b) kinetic SZ effect; (c) thermal SZ effect; (d) Galactic dust; (e) Galactic free-free; (f) Galactic synchrotron emission. Each component is plotted at 300 GHz and has been convolved with a Gaussian beam of FWHM equal to 4.5 arcmin. The map units are equivalent thermodynamic temperature in  $\mu\text{K}$ .



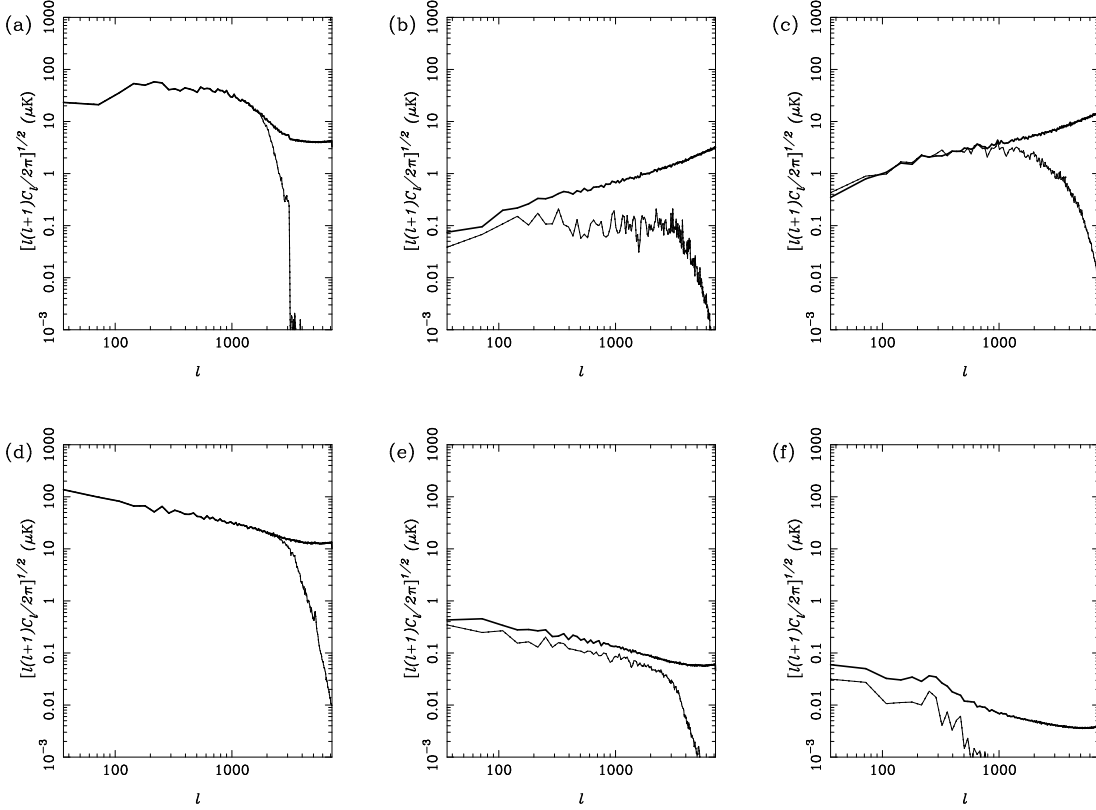


**Figure 5.** The power spectra of the input maps (bold line) compared to the power spectra of the maps reconstructed using MEM (thin line). In this case the component separation was performed assuming knowledge of the individual power spectra of the input components.

**Table 2.** The rms of the residuals per 4.5 arcmin FWHM Gaussian beam (in  $\mu\text{K}$ ) of the MEM reconstructions in the presence and absence of point sources, assuming no power spectrum information.

Component	$e_{\text{rms}}$ no sources	$e_{\text{rms}}$ with sources
CMB	6.10	8.70
Kinetic SZ	2.68	2.70
Thermal SZ	4.35	5.80
Dust	1.90	4.80
Free-Free	0.44	1.60
Synchrotron	0.07	0.23

In Table 2 we compare the rms residuals,  $e_{\text{rms}}$ , per 4.5 arcmin FWHM Gaussian beam, of the reconstructions shown in Fig. 6 with the corresponding results obtained in Paper I in the absence of point sources. We see that the value of the  $e_{\text{rms}}$  has increased for all the components with respect to the case when point sources are not present in the simulations. Nevertheless, the relative errors for the CMB, thermal SZ and Galactic dust components are still reasonably small. In particular, we note that even in this pessimistic scenario, the rms error on the CMB reconstruction is still only  $8.7 \mu\text{K}$ .

Finally, in Fig. 7 we plot the power spectra of the reconstructed maps and compare them with the input power spectra. For the CMB (panel a), we see that the reconstructed power spectrum again follows the true spectrum very closely up to  $\ell \approx 1800$ , at which point it drops directly to zero. The dust power spectrum (panel d) is also very accurately recovered up to  $\ell \approx 2500$ . For the thermal SZ ef-

fect (panel c) follows the true spectrum up to  $\ell \approx 200$ , but then begins gradually to overestimate the true spectrum before dropping to zero at  $\ell \approx 1200$ . The additional power in the reconstructed power spectrum is a result of misidentifying point sources as thermal SZ effects from clusters. As expected from the reconstructed maps shown in Fig. 6, the power spectra of the true kinetic SZ, free-free and synchrotron emission are not recovered and the reconstructed free-free and synchrotron power spectra oscillate widely about the true spectrum before dropping to zero at  $\ell \approx 300$ . We again find that the true power spectrum in each case lies within the estimated one-sigma errors on the reconstructed power spectrum at all multipoles.

We note that for the CMB and dust components the power spectra are apparently recovered over a larger range of multipoles than when point sources were not included in the analysis (see Paper I). The reason for this becomes clear if we include full power spectrum information for the six input components shown in Fig. 1, but do not include the point source contribution in the noise covariance matrix. In this case, the reconstructed power spectra of the CMB and dust are overestimated and possess a distinct bump in the multipole range  $\ell \approx 1500\text{--}2500$  and  $\ell \approx 2500\text{--}3500$  respectively. This feature is due to the contribution to high multipoles of the point sources. We must be careful when interpreting the power spectra of the recovered maps at high multipoles, since these angular scales may be contaminated by point source emission despite the fact that only a few point sources are obvious in the reconstructed maps.



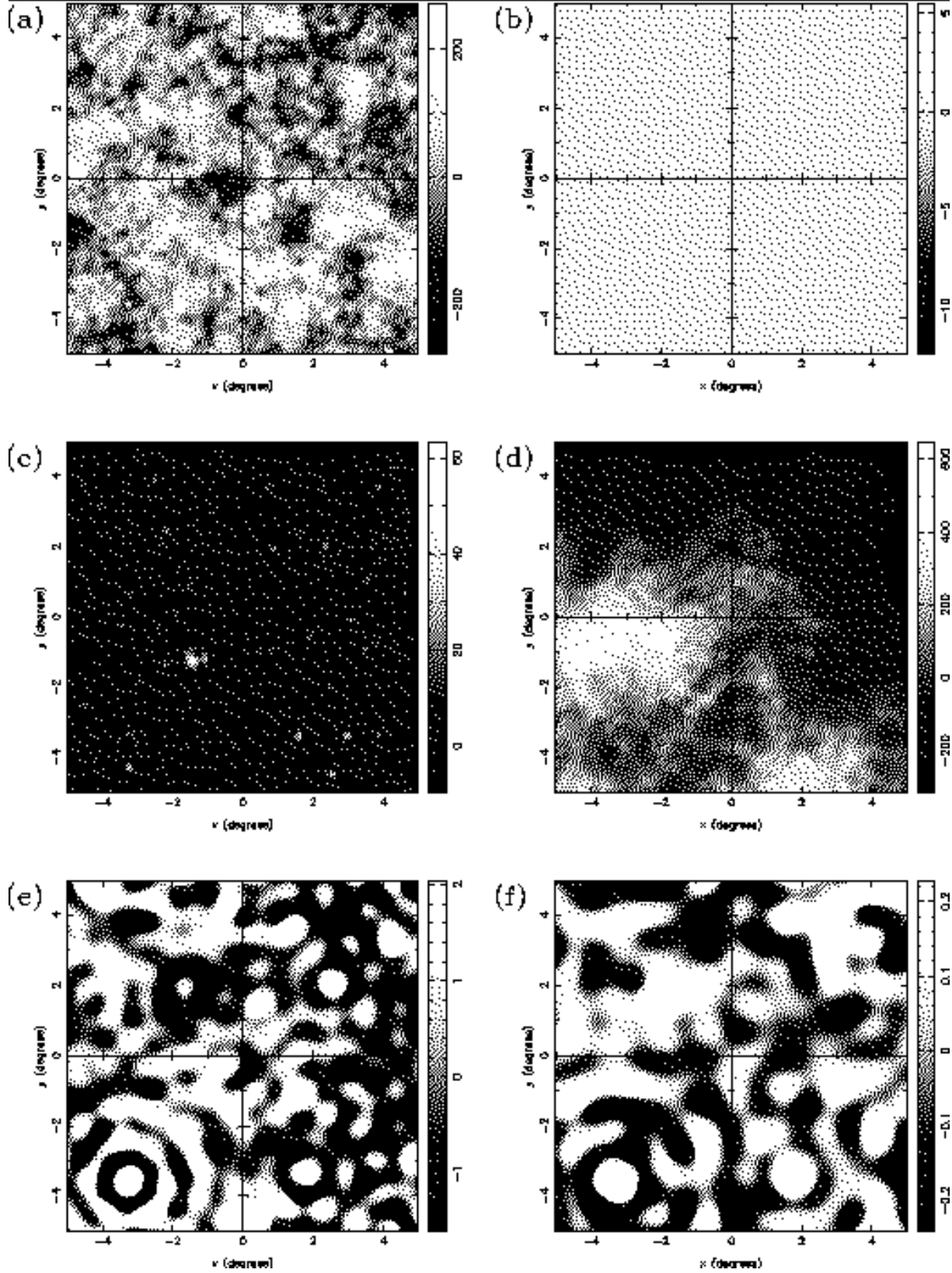


**Figure 6.** MEM reconstruction of the  $10 \times 10 \text{ deg}^2$  maps of the input components shown in Fig. 1, using no power spectrum information (see text). The components are: (a) primary CMB fluctuations; (b) kinetic SZ effect (c) thermal SZ effect; (d) Galactic dust; (e) Galactic free-free; (f) Galactic synchrotron emission. Each component is plotted at 300 GHz and has been convolved with a Gaussian beam of FWHM equal to 4.5 arcmin. The map units are equivalent thermodynamic temperature in  $\mu\text{K}$ .

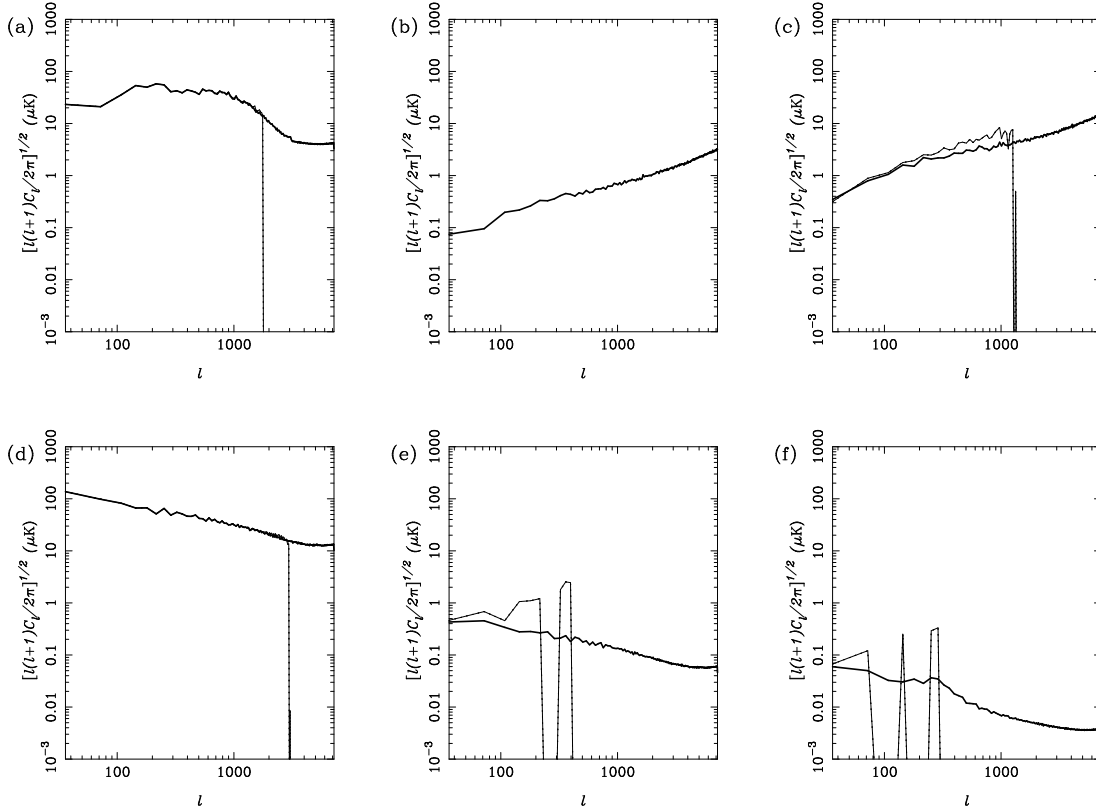


**Figure 7.** The power spectra of the input maps (bold line) compared to the power spectra of the maps reconstructed using MEM with no power spectrum information (thin line). In panel (b) only the input power spectrum is shown for the kinetic SZ effect, since the reconstructed map in this case is everywhere zero.

#### 4 RECOVERY OF POINT SOURCE CATALOGUES

We have so far concerned ourselves primarily with the reconstruction of the CMB and other foreground emission in the presence of point sources. Nevertheless, an additional aim of the Planck Surveyor mission is to compile point source catalogues over a wide range of frequencies. In this section we therefore investigate how accurately we can recover the input point source population used in the simulations.

It is clear that the generalised MEM approach discussed in Section 2 has in no way been optimised to achieve the goal of recovering point sources. Indeed, the mechanism for preventing the inclusion of sources into the reconstructed CMB and diffuse foreground maps was to regard the sources as an additional noise component. Nevertheless, given the absence of point sources in the reconstructions shown in Figs 4 & 6, it is clear that some information concerning these sources can be recovered by comparing the reconstructions with the input data.

We use the following straightforward technique to obtain information about the point source distribution at each Planck Surveyor observing frequency. We first make simulated data at each frequency using the MEM reconstructions as inputs (as opposed to true maps shown in Fig. 1). For each observing frequency the MEM reconstruction of each physical components is projected in frequency using its known spectral behaviour. The resulting maps are then added together to produce the MEM reconstruction of the sky at this frequency in the absence of point sources. This map is then convolved with the appropriate Planck Surveyor observing beam to produce mock data at this frequency. These mock data are then subtracted from the true input data (which contain the point

source contribution). Since the MEM reconstructions contain very few point sources, we thus hope to recover an approximate point source map at each Planck Surveyor observing frequency.

Using the MEM reconstructions shown in Fig 4, which assume full power spectrum information, we find that the recovered point source maps are quite accurate. For the sake of brevity we display only the reconstructions for the 44 and 353 GHz channels, which are shown in Figs 8 & 9 respectively. These channels are chosen simply because they lie near the centres of the frequency ranges of the LFI and HFI respectively. We emphasise that these maps represent the point sources as observed by the Planck Surveyor, i.e. convolved with the appropriate observing beam.

In Fig. 8, we see that at 44 GHz the reconstructed point source map in panel (b) is very similar to the input map in shown in panel (a). Indeed all of the prominent point sources have been recovered at approximately the correct flux. There is, however, some evidence of residual diffuse emission in the top left-hand corner of the recovered map. We quantify the point source recovery by identifying and extracting point sources from the input and recovered maps using the SExtractor algorithm (Bertin & Arnouts 1996). This algorithm first fits an unresolved background to an image and then identifies point sources superposed on this background. Using the standard default settings, SExtractor fitted an unresolved background with mean level 0.05 Jy per beam area to both the true and recovered point source maps shown in Fig. 8(a) and (b). After subtracting this background, the resulting rms fluctuation was found to be 0.01 Jy for each map and SExtractor then identified sources down to this level. Thus the detection flux limit in each case was 0.06 Jy. For the input map, 93 sources were found as compared to 85 for the recov-

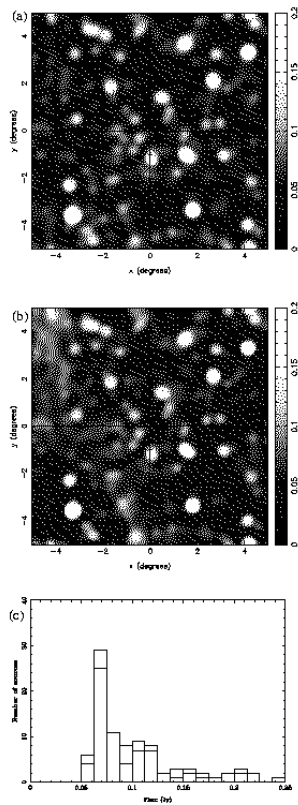


**Figure 8.** (a) The input point source map at 44 GHz convolved with the appropriate Planck Surveyor observing beam. (b) The recovered point source map at 44 GHz. (c) A histogram of point source fluxes for the input map (heavy line) and recovered map (faint line) obtained using SExtractor; see text for details. The greyscales in (a) and (b) are flux density in Jy

ered map. The resulting histograms of source counts for the input map (heavy line) and the recovered map (faint line) are shown in Fig. 8(c) and are clearly very similar.

In Fig. 9, we show the results for the 353 GHz. Since the FWHM of the observing beam at this frequency is only 4.5 arcmin, the number of distinguishable point sources is much higher than at 44 GHz. We note once more that the input and reconstructed point source maps are very similar. Indeed, even very faint sources are accurately recovered. SExtractor again fitted an unresolved background component with mean value 0.05 Jy per beam area to both maps, resulting in a residual rms fluctuation of 0.01 Jy in each case. Thus, as for the 44 GHz channel, the detection flux limit was 0.06 Jy. The algorithm identified 1869 sources in the true map and 1676 sources in the recovered map. The histograms of the point source counts are shown in Fig. 9(c) and are seen to agree reasonably well. There is, however, some evidence that the recovered map has too few sources in the range 0.10–0.12 Jy and too many in the range 0.06–0.08 Jy. This is most likely caused by some of the flux associated with the point sources being incorrectly assigned to very low-level diffuse foreground emission by the MEM separation algorithm.

The results at other observing frequencies are of similar quality to those shown in Figs 8 & 9. We thus find that the input point source catalogues at each Planck Surveyor frequency can be recovered to reasonable accuracy using the above method. We re-

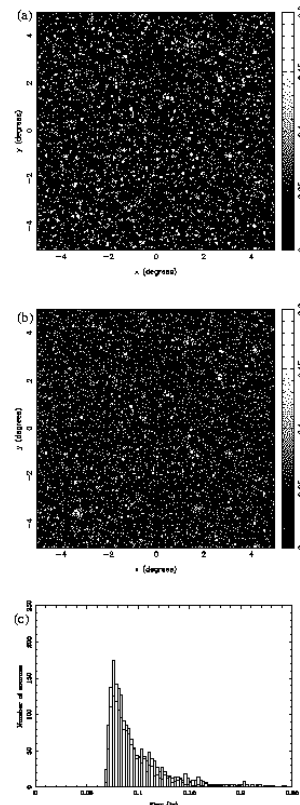


**Figure 9.** As for Fig. 8 but for the 353 GHz Planck Surveyor frequency channel.

emphasise that this has been achieved with no direct subtraction of point sources from the data, but instead by the application of the MEM separation algorithm in which the point sources were considered as an extra ‘noise’ contribution.

The recovered point source maps discussed above were created using the MEM reconstructions obtained by assuming full power spectrum information. Nevertheless, we find that the results are not appreciably affected by using the MEM reconstructions obtained assuming no power spectrum information shown in Fig. 6. At the lower LFI frequencies the flux of the brightest sources is underestimated by about a factor of two since some of flux has been misidentified by MEM as synchrotron or free-free emission. In the HFI frequency range, however, the dominant diffuse emission is due to the CMB and Galactic dust, which are both accurately reconstructed, and the resulting point source recovery is of a similar quality to that shown in Fig. 9.

## 5 DISCUSSION AND CONCLUSIONS

In this paper we study the effect of point sources on the reconstruction of CMB anisotropies and foreground emission from simulated satellite observations. In particular, we apply a generalised form of the maximum-entropy method (MEM) developed in Hobson et al. (1998) to analyse simulated observations by the Planck Surveyor satellite of a  $10 \times 10 \text{ deg}^2$  patch of sky.

We do not attempt to remove contaminated pixel from the data, but instead introduce information about the power spectrum

of the point sources in each frequency channel and the correlations between frequencies. The resulting reconstructions show that, even in the presence of contaminating point sources, the CMB emission can still be recovered with an accuracy of about  $8 \mu\text{K}$ , even for the pessimistic scenario in which we assume no prior information about the covariance structure of the sky emission. It is possible that this accuracy could be improved by a suitable scheme for removing point sources from the data before the MEM component separation algorithm is applied. Moreover, given some prior knowledge of the power spectra of the CMB and foregrounds, not only can the accuracy of the CMB reconstruction be improved, but it is possible to obtain accurate reconstructions of the thermal SZ effect from clusters and the Galactic dust, free-free and synchrotron emission. The kinetic SZ effect may also be recovered in clusters that have a large thermal effect.

As a final point, we find that by using the MEM reconstructions of the CMB and foreground components it is possible to subtract simulated mock data from the true data in order to recover the point source contribution at each of the Planck Surveyor observing frequencies. The recovered point source maps can then be analysed using, for example, the SExtractor algorithm in order to compile point source catalogues.

## ACKNOWLEDGEMENTS

JLS and RBB acknowledge financial support from the Spanish DGES, project PB95-1132-C02-02, CICYT, project ESP96-2798-E and from Comisión Mixta Caja Cantabria-Universidad de Cantabria. RBB acknowledges a Spanish M.E.C. Ph.D. scholarship and expresses her gratitude to the Mullard Radio Astronomy Observatory for its hospitality during her stay there. LT acknowledges partial financial support from the Spanish DGES, project PB95-1132-C02-02 and by the Agenzia Spaziale Italiana (ASI). LT also benefited from many years of collaboration on foregrounds with L. Danese, G. De Zotti, A. Franceschini and C. Burigana. FRB thanks R. Gispert for permission to use some of their unpublished results. We also thank E. Martínez-González, L. Cayón, and F. Argüeso-Gómez for their useful comments.

## REFERENCES

- Bersanelli M. et al., 1996, Report on Phase A Study for COBRAS/SAMBA, European Space Agency.
- Bertin E., Arnouts S., 1996, *A&AS*, 117, 393
- Bouchet F.R., Gispert R., Boulanger F., Puget J.L., 1997, in Bouchet F.R., Gispert R., Guideroni B., Tran Thanh Van J., eds, Proc. 36th Moriond Astrophysics Meeting, Microwave Anisotropies. Editions Frontière, Gif-sur-Yvette, p. 481
- Burigana C., Danese L., De Zotti G., Franceschini A., Mazzei P., Toffolatti L., 1997, *MNRAS*, 287, L17
- Danese L., De Zotti G., Franceschini A., Toffolatti L., 1987, *ApJ*, 318, L15
- Franceschini A., Mazzei P., De Zotti G., Danese L., 1994, *ApJ*, 427, 140
- Gispert R., Bouchet F.R., 1997, in Bouchet F.R., Gispert R., Guideroni B., Tran Thanh Van J., eds, Proc. 36th Moriond Astrophysics Meeting, Microwave Anisotropies. Editions Frontière, Gif-sur-Yvette, p. 503
- Hobson M.P., Jones A.W., Lasenby A.N., Bouchet, F. 1998 *MNRAS*, in press (Paper I)
- Press P. H., Teukolsky S. A., Vetterling W. T., Flannery B. P., 1994, *Numerical Recipes*. Cambridge Univ. Press, Cambridge
- Puget J.-L., Abergel A., Bernard J.-P., Boulanger F., Burton W.B., Désert F.-X., Hartmann D., 1996, *A&A*, 308, L5

- Tegmark M., de Oliveira-Costa A., 1998, *ApJ*, submitted (astro-ph/9802123)
- Toffolatti L., Argüeso Gómez F., De Zotti G., Mazzei P., Franceschini A., Danese L., Burigana C., 1998, *MNRAS*, 297, 117

This paper has been produced using the Royal Astronomical Society/Blackwell Science L<sup>A</sup>T<sub>E</sub>X style file.